Advances in Applied Mathematics and Mechanics
Adv. Appl. Math. Mech., Vol. **5**, No. 4, pp. 510-527

DOI: 10.4208/aamm.13-13S07
August 2013

A Moving Pseudo-Boundary MFS for Three-Dimensional Void Detection

Andreas Karageorghis[1,*], Daniel Lesnic[2] and Liviu Marin[3]

[1] *Department of Mathematics and Statistics, University of Cyprus, P.O. Box 20537, 1678 Nicosia, Cyprus*
[2] *Department of Applied Mathematics, University of Leeds, Leeds LS2 9JT, UK*
[3] *Institute of Solid Mechanics, Romanian Academy, 15 Constantin Mille, P.O.Box 1-863, 010141 Bucharest, and Centre for Continuum Mechanics, Faculty of Mathematics and Computer Science, University of Bucharest, 14 Academiei, 010014 Bucharest, Romania*

Received 10 May 2012; Accepted (in revised version) 8 September 2012

Available online 7 June 2013

Dedicated to Graeme Fairweather on the occasion of his 70th birthday. Mentor and friend for many years.

Abstract. We propose a new moving pseudo-boundary method of fundamental solutions (MFS) for the determination of the boundary of a three-dimensional void (rigid inclusion or cavity) within a conducting homogeneous host medium from overdetermined Cauchy data on the accessible exterior boundary. The algorithm for imaging the interior of the medium also makes use of radial spherical parametrization of the unknown star-shaped void and its centre in three dimensions. We also include the contraction and dilation factors in selecting the fictitious surfaces where the MFS sources are to be positioned in the set of unknowns in the resulting regularized nonlinear least-squares minimization. The feasibility of this new method is illustrated in several numerical examples.

AMS subject classifications: 65N35, 65N21, 65N38

Key words: Void detection, inverse problem, method of fundamental solutions.

1 Introduction

An important subclass of inverse problems very often encountered in real life applications is represented by so-called inverse geometric problems. In such problems, the governing equation, material properties, boundary conditions and a portion of the geometry

*Corresponding author.
Email: andreask@ucy.ac.cy (A. Karageorghis), amt5ld@maths.leeds.ac.uk (D. Lesnic), marin.liviu@gmail.com (L. Marin)

that is accessible are all known, whilst the portion of the geometry that is hidden from view is to be characterized with the help of an over-specified (Cauchy) condition on the exposed accessible surface. More precisely, in this paper we refer to applications in the nondestructive evaluation of three-dimensional voids (rigid inclusions and cavities) associated with isotropic steady-state heat conduction (i.e., Laplace's equation), for which both the boundary temperature and the heat flux are measured on the accessible exposed surface, the boundary condition on the void surface is known, while the geometry of the void is to be determined. This situation also occurs in electrical impedance tomography (EIT) where the boundary temperature and heat flux are replaced by the voltage and current flux, respectively. This inverse geometric problem has been solved by a variety of mesh dependent numerical methods, such as the finite difference (FDM), finite element (FEM) and boundary element (BEM) methods, see e.g., [7, 8, 15, 16, 23–25], and its numerical solution is, arguably, the most computationally intensive among problems belonging to the general class of inverse problems. Its inherent nature requires a complete regeneration of the mesh as the geometry evolves regardless of whether a numerical or analytical approach is employed to solve the associated direct problem. Consequently, the solution of inverse geometric problems via these traditional numerical methods is seriously dependent on the quality of the mesh since a simple topological mesh would cause the solution to be distorted and fails to complete the inverse calculation. Moreover, obtaining a high-quality mesh requires tedious (re)meshing in the inverse iterative process. Therefore, it is of crucial importance to find a proper and efficient numerical method to solve the inverse geometric problem under investigation in a stable and accurate manner.

The method of fundamental solutions (MFS) was first introduced as a numerical technique for direct problems in the late seventies in a paper by Mathon and Johnston [26] followed by applications to potential problems in papers by Fairweather and Johnston [10, 17]. In recent years, it has been used extensively for the numerical solution of various types of inverse problems, mainly because of the ease with which it can be implemented, see the recent survey papers [21, 22]. There are two MFS approaches related to the location of the MFS singularities (one of the most important issues concerning this meshless method). In the *static approach*, the singularities are pre-assigned and kept fixed throughout the solution process, whilst in the *dynamic approach*, the singularities and the unknown MFS coefficients are determined simultaneously during the solution process [9]. Because the coordinates of the singularities appear non-linearly, this approach leads to a non-linear least squares minimization problem. The obvious criticism of this approach is that in the case of linear boundary value problems one is required to solve a non-linear discrete problem at a high cost. On the other hand, the optimal placement of the singularities in the static approach is a major issue, see e.g., [2].

The detection of two-dimensional cavities and inclusions was investigated using a regularized MFS and the static approach in [3, 4, 18, 19]. Recently, the authors have proposed a dynamic moving pseudo-boundary MFS for void detection in two dimensions [20]. The purpose of this study is to extend and numerically implement this method to three-dimensional void detection problems. The paper is organized as follows. In Sec-

tion 2 we present the mathematical formulation of the problem. The MFS approximation for this problem is described in Section 3, while the implementational details are given in Section 4. Several numerical examples are investigated in Section 5. Finally, some comments and conclusions are given in Section 6.

2 Mathematical formulation

In this section we formulate the direct and inverse problems related to a rigid inclusion or a cavity. The direct problem given by the Laplace equation

$$\Delta u = 0 \quad \text{in } \Omega, \tag{2.1a}$$

subject to the Dirichlet boundary condition

$$u = f \quad \text{on } \partial\Omega_2, \tag{2.1b}$$

and the homogeneous boundary condition

$$\alpha u + (1-\alpha)\partial_\nu u = 0 \quad \text{on } \partial\Omega_1, \quad \text{where } \alpha \in \{0,1\}, \tag{2.1c}$$

has a unique weak solution $u \in \mathcal{H}^1(\Omega)$ if $f \in \mathcal{H}^{1/2}(\partial\Omega_2)$, and a unique classical solution $u \in \mathcal{C}^2(\Omega)\cap\mathcal{C}(\bar{\Omega})$, provided f is sufficiently smooth. In the above, $\Omega = \Omega_2 \setminus \Omega_1$, where $\overline{\Omega}_1 \subset \Omega_2$, is a bounded annular domain with boundary $\partial\Omega = \partial\Omega_1 \cup \partial\Omega_2$. The void Ω_1 may have many connected components, but Ω should be connected. Eq. (2.1c), covers both Dirichlet ($\alpha = 1$, i.e., Ω_1 is a rigid inclusion) and Neumann ($\alpha = 0$, i.e., Ω_1 is a cavity) boundary conditions on $\partial\Omega_1$.

The inverse problem we are concerned with consists of determining not only the function u, but also the inclusion Ω_1 so that u satisfies the Laplace equation (2.1a), the given Dirichlet data $f \not\equiv$ constant in (2.1b), the homogeneous boundary condition (2.1c) and the Neumann current flux measurement

$$g := \partial_\nu u \quad \text{on } \partial\Omega_2. \tag{2.1d}$$

In (2.1c) and (2.1d), the vector $\boldsymbol{\nu}$ denotes the outward unit normal to the annular domain Ω.

In the inverse problem, the fact that the location of Ω_1 is not known is compensated by the additional boundary condition (2.1d). When $\alpha = 0$, for (2.1a), (2.1c) and (2.1d) to be consistent, we require

$$\int_{\partial\Omega_2} g(s)ds = 0. \tag{2.2}$$

In contrast to the direct linear and well-posed boundary value problem (2.1a)-(2.1c) with Ω_1 known, the inverse problem (2.1a)-(2.1d) with Ω_1 unknown is nonlinear and ill-posed. Although the solution is unique, see [12] for two dimensions and [1] for three dimensions, it is unstable with respect to small errors in the input Cauchy data (2.1b) and (2.1d).

3 The method of fundamental solutions (MFS)

In the application of the MFS to (2.1), we seek an approximation to the solution of the three-dimensional Laplace's equation (2.1a) as a linear combination of fundamental solutions in the form

$$u_{NM}(\boldsymbol{c}^1,\boldsymbol{c}^2,\boldsymbol{\xi}^1,\boldsymbol{\xi}^2;\boldsymbol{x})=\sum_{s=1}^{2}\sum_{n=1}^{N}\sum_{m=1}^{M}c_{n,m}^{s}G(\boldsymbol{\xi}_{n,m}^{s},\boldsymbol{x}),\quad \boldsymbol{x}\in\overline{\Omega}, \tag{3.1}$$

where G is the fundamental solution of the three-dimensional Laplace equation, given by

$$G(\boldsymbol{\xi},\boldsymbol{x})=\frac{1}{4\pi}\frac{1}{|\boldsymbol{\xi}-\boldsymbol{x}|}. \tag{3.2}$$

The sources $(\boldsymbol{\xi}_{n,m}^{s})_{n=\overline{1,N},m=\overline{1,M},s=\overline{1,2}}$ are located outside the solution domain Ω, i.e., in $\Omega_1\cup(\mathbb{R}^3\setminus\bar{\Omega}_2)$. In particular, the sources $(\boldsymbol{\xi}_{n,m}^{1})_{n=\overline{1,N},m=\overline{1,M}}\in\Omega_1$ are placed on a (moving) pseudo-boundary $\partial\Omega_1'$ similar (contraction) to $\partial\Omega_1$, while the sources $(\boldsymbol{\xi}_{n,m}^{2})_{n=\overline{1,N},m=\overline{1,M}}\in\mathbb{R}^3\setminus\overline{\Omega}_2$ are placed on a pseudo-boundary $\partial\Omega_2'$ similar (dilation) to $\partial\Omega_2$. In the MFS, taking the pseudo-boundary similar to the boundary yields, in general, improved results as has been demonstrated by Gorzelańczyk and Kołodziej [11]. In (3.1), the singularities $(\boldsymbol{\xi}_{n,m}^{2})_{n=\overline{1,N},m=\overline{1,M}}$ are *not* preassigned. Also, the sources $(\boldsymbol{\xi}_{n,m}^{1})_{n=\overline{1,N},m=\overline{1,M}}$ move with $\partial\Omega_1$, as will be described in the iterative process presented in the sequel. The fact that the locations of the pseudo-boundaries $\partial\Omega_1'$ and $\partial\Omega_2'$ are determined as part of the solution takes care of the inherent problem of optimally locating the sources in the MFS.

Without loss of generality, we shall assume that the (known) fixed exterior boundary $\partial\Omega_2$ is a sphere of radius R. As a result, the outer boundary collocation and source points are chosen as

$$\boldsymbol{x}_{k,\ell}^{2}=R\big(\sin\tilde{\vartheta}_k\cos\tilde{\phi}_\ell,\sin\tilde{\vartheta}_k\sin\tilde{\phi}_\ell,\cos\tilde{\vartheta}_k\big),\qquad k=\overline{1,\tilde{N}},\qquad \ell=\overline{1,\tilde{M}}, \tag{3.3a}$$

$$\boldsymbol{\xi}_{n,m}^{2}=\eta_{ext}R\big(\sin\vartheta_n\cos\phi_m,\sin\vartheta_n\sin\phi_m,\cos\vartheta_n\big),\qquad n=\overline{1,N},\qquad m=\overline{1,M}, \tag{3.3b}$$

respectively, where

$$\tilde{\vartheta}_k=\frac{\pi k}{\tilde{N}+1},\quad k=\overline{1,\tilde{N}},\quad \tilde{\phi}_\ell=\frac{2\pi(\ell-1)}{\tilde{M}},\quad \ell=\overline{1,\tilde{M}},$$

and

$$\vartheta_n=\frac{\pi n}{N+1},\quad n=\overline{1,N},\quad \phi_m=\frac{2\pi(m-1)}{M},\quad m=\overline{1,M},$$

and the (unknown) parameter $\eta_{ext}\in(1,S)$ with $S>1$ prescribed.

We further assume that the unknown boundary $\partial\Omega_1$ is a smooth, star-like surface with respect to its centre which has unknown coordinates (X,Y,Z). This means that its

equation in spherical coordinates can be written as

$$x=X+r(\vartheta,\phi)\sin\vartheta\cos\phi,\quad y=Y+r(\vartheta,\phi)\sin\vartheta\sin\phi,\quad z=Z+r(\vartheta,\phi)\cos\vartheta,$$
$$\vartheta\in(0,\pi),\quad \phi\in[0,2\pi),\quad \text{where } r \text{ is a smooth } 2\pi-\text{periodic function.} \tag{3.4}$$

The discretised form of (3.4) for $\partial\Omega_1$ becomes

$$r_{n,m}=r(\vartheta_n,\phi_m),\quad n=\overline{1,N},\quad m=\overline{1,M}, \tag{3.5}$$

and we choose the inner boundary collocation and source points as

$$\boldsymbol{x}^1_{n,m}=(X,Y,Z)+r_{n,m}\big(\sin\vartheta_n\cos\phi_m,\sin\vartheta_n\sin\phi_m,\cos\vartheta_n\big),\qquad n=\overline{1,N},\quad m=\overline{1,M}, \tag{3.6a}$$
$$\boldsymbol{\xi}^1_{m,n}=(X,Y,Z)+\eta_{int}r_{n,m}\big(\sin\vartheta_n\cos\phi_m,\sin\vartheta_n\sin\phi_m,\cos\vartheta_n\big),\quad n=\overline{1,N},\quad m=\overline{1,M}, \tag{3.6b}$$

where the (unknown) parameter $\eta_{int}\in(0,1)$.

4 Implementational details

The coefficients $(c^1_{n,m})_{n=\overline{1,N},m=\overline{1,M}}$, $(c^2_{n,m})_{n=\overline{1,N},m=\overline{1,M}}$ in (3.1), the radii $(r_{n,m})_{n=\overline{1,N},m=\overline{1,M}}\in(0,1)$ in (3.5), the contraction and dilation coefficients η_{int} and η_{ext} in (3.6b) and (3.3b), and the coordinates of the centre (X,Y,Z) can be determined by imposing the boundary conditions (2.1b), (2.1c) and (2.1d) in a regularized least-squares sense. This leads to the minimization of the functional

$$\begin{aligned}S(\boldsymbol{c}^1,\boldsymbol{c}^2,\boldsymbol{r},\boldsymbol{\eta},\boldsymbol{C}):=&\sum_{n=1}^{\tilde N}\sum_{m=1}^{\tilde M}\Big[u_{NM}(\boldsymbol{c}^1,\boldsymbol{c}^2,\boldsymbol{\xi}^1,\boldsymbol{\xi}^2;\boldsymbol{x}^2_{n,m})-f^\varepsilon(\boldsymbol{x}^2_{n,m})\Big]^2\\
&+\sum_{n=1}^{\tilde N}\sum_{m=1}^{\tilde M}\Big[\partial_\nu u_{NM}(\boldsymbol{c}^1,\boldsymbol{c}^2,\boldsymbol{\xi}^1,\boldsymbol{\xi}^2;\boldsymbol{x}^2_{n,m})-g^\varepsilon(\boldsymbol{x}^2_{n,m})\Big]^2\\
&+\sum_{n=1}^{N}\sum_{m=1}^{M}\Big[\alpha u_{NM}(\boldsymbol{c}^1,\boldsymbol{c}^2,\boldsymbol{\xi}^1,\boldsymbol{\xi}^2;\boldsymbol{x}^1_{n,m})+(1-\alpha)\partial_\nu u_{NM}(\boldsymbol{c}^1,\boldsymbol{c}^2,\boldsymbol{\xi}^1,\boldsymbol{\xi}^2;\boldsymbol{x}^1_{n,m})\Big]^2\\
&+\lambda_1\big\{|\boldsymbol{c}^1|^2+|\boldsymbol{c}^2|^2\big\}+\lambda_2\Big(\sum_{n=1}^{N}\sum_{m=2}^{M}\Big(\frac{r_{n,m}-r_{n,m-1}}{2\pi/M}\Big)^2\\
&+\sum_{n=2}^{N}\sum_{m=1}^{M}\Big(\frac{r_{n,m}-r_{n-1,m}}{\pi/(N+1)}\Big)^2\Big),\end{aligned} \tag{4.1}$$

where $\lambda_1,\lambda_2\geq 0$ are regularization parameters to be prescribed, $\boldsymbol{c}^1=[c^1_{1,1},c^1_{1,2},\ldots,c^1_{N,M}]^T$, $\boldsymbol{c}^2=[c^2_{1,1},c^2_{1,2},\ldots,c^2_{N,M}]^T$, $\boldsymbol{r}=[r_{1,1},r_{1,2},\ldots,r_{N,M}]^T$, $\boldsymbol{\eta}=[\eta_{int},\eta_{ext}]^T$, $\boldsymbol{C}=[X,Y,Z]^T$, and the superscript ^{T} denotes the transpose.

Remark 4.1. (i) The Dirichlet data (2.1b) and the current flux data (2.1d) come from practical measurements which are inherently contaminated with noisy errors, and that is why we have replaced f and g by f^ε and g^ε, respectively, where, in computation, the noisy data are generated as

$$f^\varepsilon(\boldsymbol{x}^2_{n,m})=(1+\rho_{n,m}p_f)f(\boldsymbol{x}^2_{n,m}),\ \ g^\varepsilon(\boldsymbol{x}^2_{n,m})=(1+\rho_{n,m}p_g)g(\boldsymbol{x}^2_{n,m}),\ \ n=\overline{1,\tilde{N}},\ \ m=\overline{1,\tilde{M}},\quad (4.2)$$

where p_f and p_g represent the percentage of noise added to the Dirichlet and Neumann boundary data on $\partial\Omega_2$, respectively, and $\rho_{m,n}$ is a pseudo-random noisy variable drawn from a uniform distribution in $[-1,1]$ using the `MATLAB` command `-1+2*rand(1,`$\tilde{M}\tilde{N}$`)`. In our numerical experiments it was observed that the effect of noise added to the Dirichlet boundary data was similar to that of perturbing the Neumann data. As a result in the numerical results section we only present results for noisy Neumann data, i.e., $p_g\neq 0$ and $p_f=0$. In Section 5 we shall re-denote p_g by p.

(ii) In (4.1), the outward normal vector $\boldsymbol{\nu}$ is defined as follows:

$$\boldsymbol{\nu}=\sin\vartheta\cos\phi\boldsymbol{i}+\sin\vartheta\sin\phi\boldsymbol{j}+\cos\vartheta\boldsymbol{k},\quad \text{if}\ \ \boldsymbol{x}\in\partial\Omega_2,\quad (4.3)$$

where $\boldsymbol{i}=(1,0,0)$, $\boldsymbol{j}=(0,1,0)$ and $\boldsymbol{k}=(0,0,1)$. In the case of the boundary $\partial\Omega_1$, we know that the position vector of a boundary point is given by

$$\boldsymbol{x}^1(\vartheta,\phi)=(X,Y,Z)+r(\vartheta,\phi)(\sin\vartheta\cos\phi,\sin\vartheta\sin\phi,\cos\vartheta),\quad (4.4)$$

and that the normal to the parametrised surface is given by

$$\boldsymbol{\nu}=\frac{\boldsymbol{x}^1_\vartheta\times\boldsymbol{x}^1_\phi}{|\boldsymbol{x}^1_\vartheta\times\boldsymbol{x}^1_\phi|},\quad (4.5)$$

where the subscripts $_\vartheta$ and $_\phi$ denote the partial derivatives with respect to ϑ and ϕ, respectively. Now,

$$\begin{aligned}\boldsymbol{x}^1_\vartheta&=\left[r_\vartheta\sin\vartheta\cos\phi+r\cos\vartheta\cos\phi,r_\vartheta\sin\vartheta\sin\phi+r\cos\vartheta\sin\phi,r_\vartheta\cos\vartheta-r\sin\vartheta\right]^T,\\ \boldsymbol{x}^1_\phi&=\left[r_\phi\sin\vartheta\cos\phi-r\sin\vartheta\sin\phi,r_\phi\sin\vartheta\sin\phi+r\sin\vartheta\cos\phi,r_\phi\cos\vartheta\right]^T,\end{aligned}$$

and thus

$$\begin{aligned}\boldsymbol{x}^1_\vartheta\times\boldsymbol{x}^1_\phi=-r\big[&-r_\phi\sin\phi+r_\vartheta\sin\vartheta\cos\vartheta\cos\phi-r\sin^2\vartheta\cos\phi,\\ &r_\phi\cos\phi+r_\vartheta\sin\vartheta\cos\vartheta\sin\phi-r\sin^2\vartheta\sin\phi,-\sin\vartheta(r_\vartheta\sin\vartheta+r\cos\vartheta)\big]^T,\end{aligned}$$

and

$$|\boldsymbol{x}^1_\vartheta\times\boldsymbol{x}^1_\phi|=r\sqrt{(r^2+r^2_\vartheta)\sin^2\vartheta+r^2_\phi},\quad (4.6)$$

yielding

$$\begin{aligned}\boldsymbol{\nu}=\frac{1}{\sqrt{(r^2+r^2_\vartheta)\sin^2\vartheta+r^2_\phi}}\big[&(-r_\phi\sin\phi+r_\vartheta\sin\vartheta\cos\vartheta\cos\phi-r\sin^2\vartheta\cos\phi)\boldsymbol{i}\\ &+(r_\phi\cos\phi+r_\vartheta\sin\vartheta\cos\vartheta\sin\phi-r\sin^2\vartheta\sin\phi)\boldsymbol{j}\\ &+(-\sin\vartheta(r_\vartheta\sin\vartheta+r\cos\vartheta))\boldsymbol{k}\big],\quad \text{if}\ \ \boldsymbol{x}\in\partial\Omega_1.\end{aligned}\quad (4.7)$$

As a result, from (3.1) and (3.2) the normal derivative $\partial_\nu u_{NM}$ is evaluated as

$$\partial_\nu u_{NM}(\boldsymbol{c}^1,\boldsymbol{c}^2,\boldsymbol{\xi}^1,\boldsymbol{\xi}^2;\boldsymbol{x})=\boldsymbol{\nu}\cdot\nabla u_{NM}=-\frac{1}{4\pi}\sum_{s=1}^{2}\sum_{n=1}^{N}\sum_{m=1}^{M}c_{n,m}^{s}\frac{(\boldsymbol{x}-\boldsymbol{\xi}_{n,m}^{s})\cdot\boldsymbol{\nu}}{|\boldsymbol{x}-\boldsymbol{\xi}_{n,m}^{s}|^3},\quad \boldsymbol{x}\in\partial\Omega, \tag{4.8}$$

where $\boldsymbol{\nu}$ is given by (4.3) and (4.7) for $\boldsymbol{x}\in\partial\Omega_2$ and $\boldsymbol{x}\in\partial\Omega_1$, respectively.

In (4.7), we use the finite-difference approximations

$$r_\phi(\vartheta_n,\phi_m)\approx\frac{r_{n,m+1}-r_{n,m-1}}{4\pi/M},\quad n=\overline{1,N},\quad m=\overline{1,M}, \tag{4.9}$$

with the convention that $r_{n,M+1}=r_{n,1}$, $r_{n,0}=r_{n,M}$, and

$$r_\vartheta(\vartheta_n,\phi_m)\approx\frac{r_{n+1,m}-r_{n-1,m}}{2\pi/(N+1)},\qquad n=\overline{2,N-1}, \tag{4.10a}$$

$$r_\vartheta(\vartheta_1,\phi_m)\approx\frac{-r_{3,m}+4r_{2,m}-3r_{1,m}}{2\pi/(N+1)},\qquad m=\overline{1,M}, \tag{4.10b}$$

$$r_\vartheta(\vartheta_N,\phi_m)\approx\frac{r_{N-2,m}-4r_{N-1,m}+3r_{N,m}}{2\pi/(N+1)},\qquad m=\overline{1,M}. \tag{4.10c}$$

(iii) Since the total number of unknowns is $3NM+5$ and the number of boundary condition collocation equations is $NM+2\tilde{N}\tilde{M}$ we need to take $\tilde{N}\tilde{M}\geq NM+3$.

(iv) Since the inverse problem is ill-posed, in (4.1), the regularization terms $\lambda_1\{|\boldsymbol{c}^1|^2+|\boldsymbol{c}^2|^2\}$ and $\lambda_2(|r_\vartheta|^2+|r_\phi|^2)$ are added in order to achieve the stability of the numerical MFS solution u_{NM} and the smooth boundary $\partial\Omega_1$. We do not include regularization terms $\lambda_3|\boldsymbol{\eta}|^2$ and $\lambda_4|\boldsymbol{C}|^2$ since both $\boldsymbol{\eta}$ and $\boldsymbol{C}$ only have a small number of components and the numerical solution is expected to be stable in both $\boldsymbol{\eta}$ and $\boldsymbol{C}$.

4.1 Non-linear minimization

The minimization of functional (4.1) is carried out using the `MATLAB` [27] optimization toolbox routine `lsqnonlin` which solves nonlinear least squares problems. This routine by default uses the so-called trust-region-reflective algorithm based on the interior-reflective Newton method [5,6], and terminates when (i) the change in the solution vector is less than a specified tolerance, or (ii) the change in the residual is less than a specified tolerance, or (iii) the specified number of iterations or number of function evaluations is exceeded. The routine `lsqnonlin` does not require the user to provide the gradient and, in addition, it offers the option of imposing lower and upper bounds on the elements of the vector of unknowns $(\boldsymbol{c}^1,\boldsymbol{c}^2,\boldsymbol{r},\boldsymbol{\eta},\boldsymbol{C})$ through the vectors `lb` and `up`. We can thus easily impose the constraints $0<r_{n,m}<1$, $n=\overline{1,N}$, $m=\overline{1,M}$, $0<\eta_{int}<1$, $1<\eta_{ext}<S$ and $-R<X<R,-R<Y<R,-R<Z<R$. In our numerical experiments we choose $S=2$. Moreover, we choose the initial guess vector of unknowns $(\boldsymbol{c}_0^1,\boldsymbol{c}_0^2,\boldsymbol{r}_0,\eta_{int}^0,\eta_{ext}^0,\boldsymbol{C})=(\boldsymbol{0},\boldsymbol{0},\boldsymbol{0}.1,0.5,2,\boldsymbol{0})$.

5 Numerical examples

Example 5.1. We first consider an example for which the exact solution is known from [4]. Here we consider the case where $X=Y=Z=0$, $R=1$ and $\alpha=1$. In particular, we consider

$$\Omega_1=\{(x,y,z)\in\mathbb{R}^3:x^2+y^2+z^2<R_0^2<1\},\quad \Omega_2=\{(x,y,z)\in\mathbb{R}^3:x^2+y^2+z^2<1\} \tag{5.1}$$

and

$$u(x,y,z)=\frac{1}{\sqrt{x^2+y^2+z^2}}-\frac{1}{R_0}. \tag{5.2}$$

For any $0<R_0<1$, the function u satisfies problem (2.1a)-(2.1d), with

$$f(x,y,z)=\frac{R_0-1}{R_0}\quad\text{and}\quad g(x,y,z)=-1,\quad (x,y,z)\in\partial\Omega_2. \tag{5.3}$$

In our numerical experiments we chose $R_0=0.5$.

In Fig. 1 we present the results obtained with no noise, no regularization with $M=N=12$, $\tilde{M}=\tilde{N}=14$ for various numbers of iterations, as well as the correct sphere to be reconstructed. From this figure it can be seen that, for exact data, very accurate numerical results are obtained in a relatively small number of iterations. Next, in order to investigate the stability of the numerical solution we perturb the input flux data g^ϵ in (4.2) by up to quite a large amount of $p_g=p=10\%$ noise. The corresponding results for noise $p=5\%$ and 10% are presented in Figs. 2 and 3, respectively. From these figures it can be seen that, if no regularization, i.e., $\lambda_1=\lambda_2=0$, is employed in the functional (4.1) which is minimized, then the numerical solution becomes unstable if the number of iterations exceeds a certain threshold which depends on the amount of noise p. In order to deal with this instability, we employ regularization in (4.1). In Figs. 4 and 5 we present the corresponding reconstructed surfaces with noise levels of $p=5\%$ and $p=10\%$, respectively, after 100 iterations, and various levels of regularization λ_1 with $\lambda_2=0$. Improved results are obtained for $\lambda_1=10^{-2}$ to 10^{-1} for $p=5\%$, and $\lambda_1=10^{-1}$ to 10^{0} for $p=10\%$. The

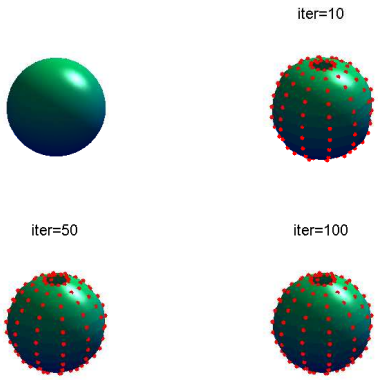

Figure 1: Example 5.1: Results for $M=N=12$, $\tilde{M}=\tilde{N}=14$, no noise and no regularization. The reconstructed values of $\boldsymbol{r}$ are presented as red dots.

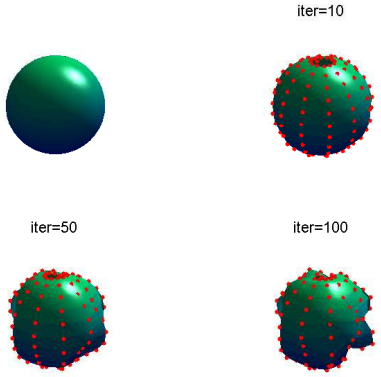

Figure 2: Example 5.1: Results for $M=N=12$, $\tilde{M}=\tilde{N}=14$, noise $p=5\%$ and no regularization.

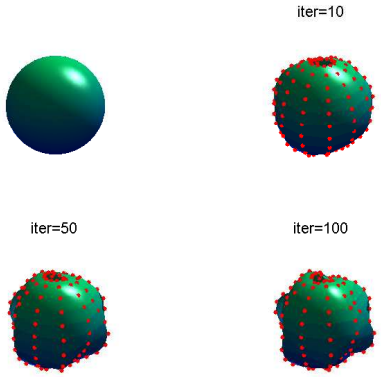

Figure 3: Example 5.1: Results for $M=N=12$, $\tilde{M}=\tilde{N}=14$, noise $p=10\%$ and no regularization.

corresponding results for various levels of regularization λ_2 with $\lambda_1=0$ are presented in Figs. 6 and 7. Improved results are obtained for $\lambda_2=10^{-2}$ to 10^0 for both $p=5\%$ and 10%.

A possible heuristic argument for how to choose the regularization parameters λ_1 or λ_2 is given by the L-curve method [13,14]. The L-curves obtained with regularization in λ_1 (when $\lambda_2=0$), and λ_2 (when $\lambda_1=0$) for $p=10\%$ noise and 100 iterations are presented in Figs. 8(a) and (b), respectively. In these figures we have denoted by $\|\boldsymbol{c}\|_2=\|(\boldsymbol{c}_1,\boldsymbol{c}_2)\|_2$ and $\|\boldsymbol{r}'\|_2=\|(\boldsymbol{r}_\vartheta,\boldsymbol{r}_\phi)\|_2$, whilst $\|\text{Residual}\|_2$ denotes the square-root of the sum of the first three terms in the right hand side of (4.1). From Figs. 8(a) and (b) one can observe that there is some indication that the corresponding L-corner values of the regularization parameters are $\lambda_1=10^{-2}$ when $\lambda_2=0$, and $\lambda_2=10^0$ when $\lambda_1=0$. The fact that these values of the regularization parameters provide stable solutions with some optimal smoothness is confirmed in Figs. 5 and 7, respectively.

Example 5.2. We next consider the case where $X=Y=Z=0$, $R=1$, $\alpha=1$ and the rigid inclusion Ω_1 has an acorn shape [28] described parametrically by

$$r(\vartheta,\phi)=0.2\big(0.6+\sqrt{4.25+2\cos 3\vartheta}\big),\quad \vartheta\in(0,\pi),\phi\in[0,2\pi), \tag{5.4}$$

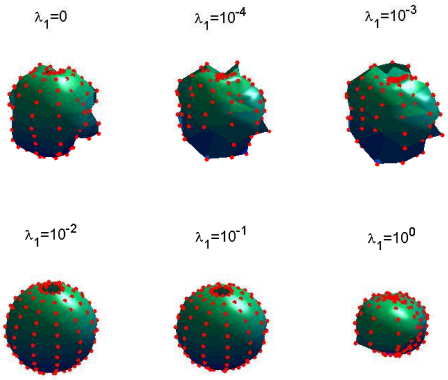

Figure 4: Example 5.1: Results for $M=N=12$, $\tilde{M}=\tilde{N}=14$, noise $p=5\%$ and regularization with λ_1.

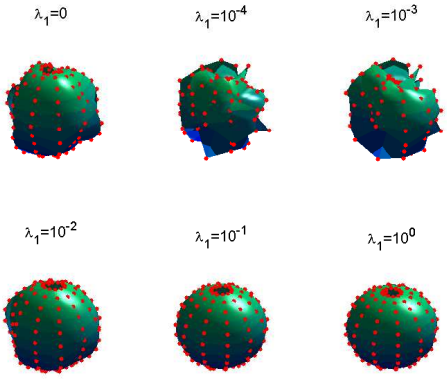

Figure 5: Example 5.1: Results for $M=N=12$, $\tilde{M}=\tilde{N}=14$, noise $p=10\%$ and regularization with λ_1.

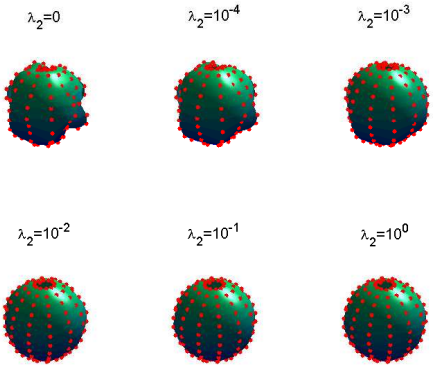

Figure 6: Example 5.1: Results for $M=N=12$, $\tilde{M}=\tilde{N}=14$, noise $p=5\%$ and regularization with λ_2.

and Ω_2 is the unit sphere. The Dirichlet data on $\partial\Omega_2$ is taken as

$$u(x,y,z)=\mathrm{e}^{x+y}, \quad (x,y,z)\in\partial\Omega_2. \tag{5.5}$$

Since in this case no analytical solution is available, the Neumann data (2.1d) is numer-

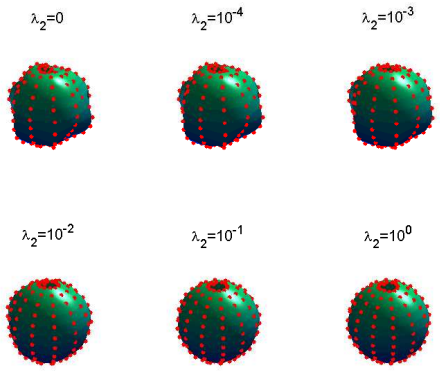

Figure 7: Example 5.1: Results for $M=N=12$, $\tilde{M}=\tilde{N}=14$, noise $p=10\%$ and regularization with λ_2.

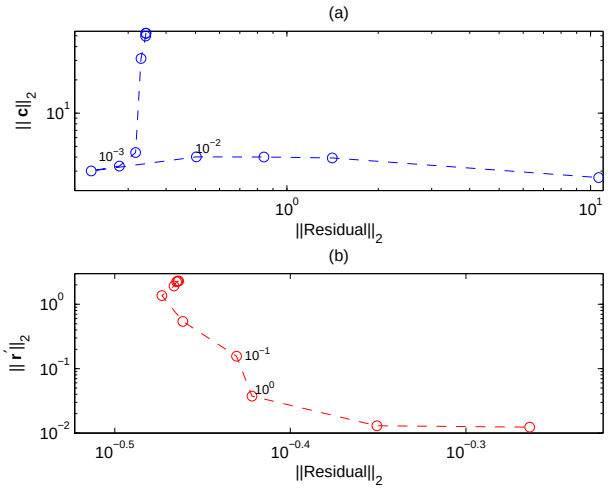

Figure 8: Example 5.1: L-curves obtained with regularization in (a) λ_1 and (b) λ_2 for noise $p=10\%$.

ically simulated by solving the direct Dirichlet well-posed problem given by Eqs. (2.1a), (5.5), and (2.1c) with $\alpha=1$, when $\partial\Omega_1$ is given by (5.4), using the MFS with $M=N=\tilde{M}=\tilde{N}=43$. In order to avoid committing an inverse crime, the inverse solver is applied using $M=N=18$, $\tilde{M}=\tilde{N}=20$. In Figs. 9 and 10 we present the results for $p=\{0,5\%\}$ noisy data, respectively, obtained with no regularization and various numbers of iterations. As in Figs. 1 and 2, it can be seen that, for exact data, very accurate numerical results are obtained with a relatively small number of iterations; however, for noisy data, unstable solutions quickly appear once the number of iterations exceeds about 100. Regularization is therefore necessary in order to alleviate this instability. In Figs. 11 and 12 we present the reconstructed surfaces for $p=5\%$ noise, obtained after 500 iterations with various levels of regularization λ_1 with $\lambda_2=0$, and λ_2 with $\lambda_1=0$, respectively. The L-curves obtained with regularization in λ_1 and λ_2 for noise $p=5\%$ and 500 iterations are presented in Figs. 13(a) and (b), respectively. First, from Fig. 13(a) it can be seen that no L-curve

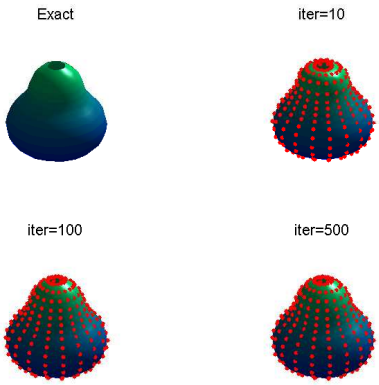

Figure 9: Example 5.2: Results for $M=N=18$, $\tilde{M}=\tilde{N}=20$, no noise and no regularization. The reconstructed values of $\boldsymbol{r}$ are presented as red dots.

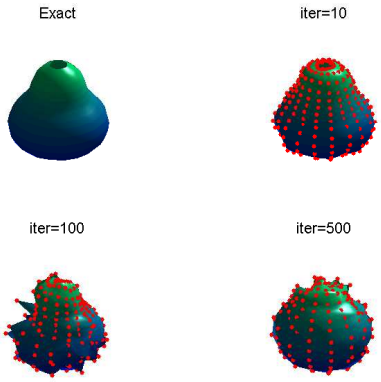

Figure 10: Example 5.2: Results for $M=N=18$, $\tilde{M}=\tilde{N}=20$, noise $p=5\%$ and no regularization.

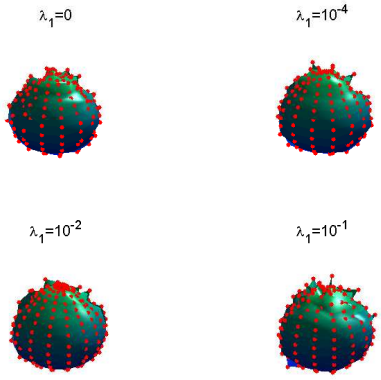

Figure 11: Example 5.2: Results for $M=N=18$, $\tilde{M}=\tilde{N}=20$, noise $p=5\%$ and regularization with λ_1.

has been obtained and, in fact, the numerical results presented in Fig. 11 show that regularization with λ_1 is not so effective. On the other hand, as can be seen from Fig. 12 and further justified by the L-corner obtained in Fig. 13(b), regularization with λ_2 between

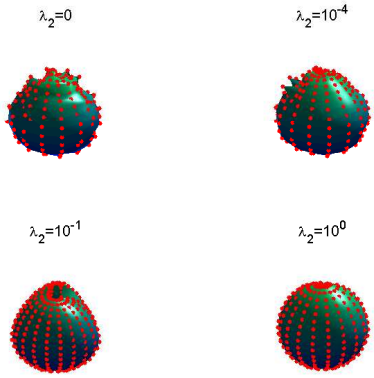

Figure 12: Example 5.2: Results for $M=N=18$, $\tilde{M}=\tilde{N}=20$, noise $p=5\%$ and regularization with λ_2.

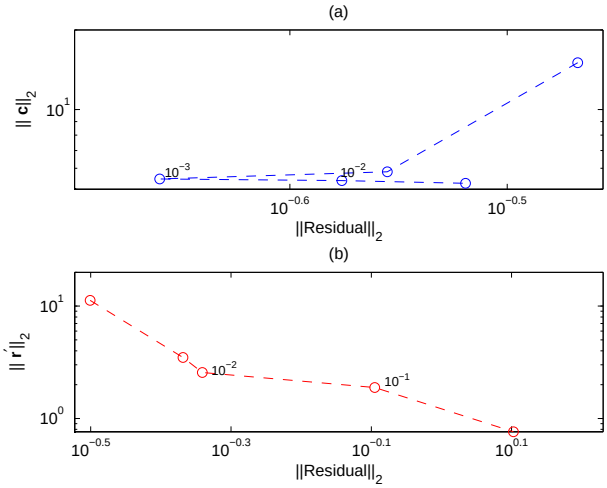

Figure 13: Example 5.2: L-curves obtained with regularization in (a) λ_1 and (b) λ_2 for noise $p=5\%$.

10^{-2} to 10^{-1} produces a stable solution which is a reasonable reconstruction of the true acorn shape (5.4).

Example 5.3. The previous two examples were related to reconstructing a rigid inclusion, i.e., $\alpha=1$ in Eq. (2.1c). In this example we consider reconstructing a cavity, i.e., $\alpha=0$ in Eq. (2.1c). We further take $X=Y=Z=0$, $R=1$, and the cavity Ω_1 has the acorn shape described parametrically by (5.4) and Ω_2 is the unit sphere. As in Example 5.2, the Dirichlet data on $\partial\Omega_2$ is taken as (5.5). Since in this case no analytical solution is available, the Neumann data (2.1d) is numerically simulated by solving the direct mixed well-posed problem given by Eqs. (2.1a), (5.5), and (2.1c) with $\alpha=0$, when $\partial\Omega_1$ is given by (5.4), using the MFS with $M=N=\tilde{M}=\tilde{N}=41$. In order to avoid committing an inverse crime, the inverse solver is applied using $M=28$, $N=14$, $\tilde{M}=\tilde{N}=20$. In Fig. 14 we present the results obtained for no noise, no regularization and various numbers of

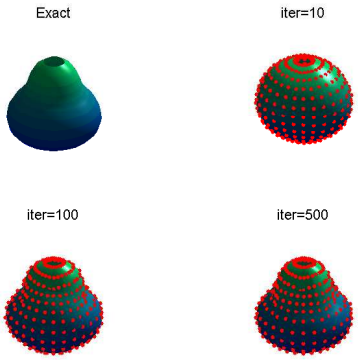

Figure 14: Example 5.3: Results for $M=28$, $N=14$, $\tilde{M}=\tilde{N}=20$, no noise and no regularization. The reconstructed values of $\boldsymbol{r}$ are presented as red dots.

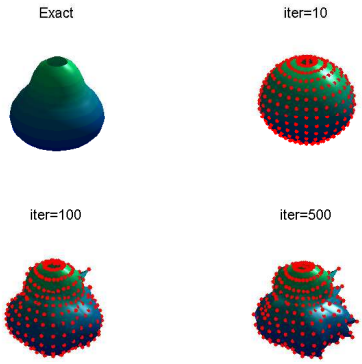

Figure 15: Example 5.3: Results for $M=28$, $N=14$, $\tilde{M}=\tilde{N}=20$, noise $p=5\%$ and no regularization.

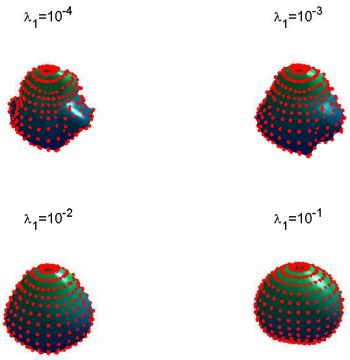

Figure 16: Example 5.3: Results for $M=28$, $N=14$, $\tilde{M}=\tilde{N}=20$, noise $p=5\%$ and regularization with λ_1.

iterations. The corresponding results for noise $p=5\%$ are presented in Fig. 15. In Figs. 16 and 17 we present the corresponding reconstructed surfaces with $p=5\%$ noise, obtained after 500 iterations, and various levels of regularization λ_1 with $\lambda_2=0$, and λ_2 with $\lambda_1=0$, respectively. Most of the conclusions drawn from Example 5.2 apply for this example as well, perhaps the only difference which is worth noting is in comparing Figs. 11 and 16

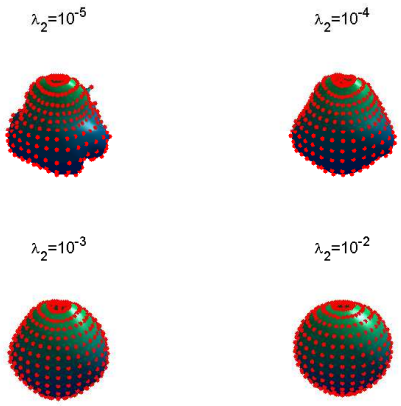

Figure 17: Example 5.3: Results for $M=28$, $N=14$, $\tilde{M}=\tilde{N}=20$, noise $p=5\%$ and regularization with λ_2.

which shows that regularization with λ_1 seems more effective when retrieving a cavity than a rigid inclusion.

Example 5.4. All the examples so far have been centred at the origin. We consider now an off-centre $X=Y=Z=0.1$ rigid inclusion Ω_1 of a pinched ball shape [28] described parametrically by

$$r(\vartheta,\phi)=0.4\sqrt{1.44+0.5(\cos 2\vartheta-1)\cos 2\phi}, \quad \vartheta\in(0,\pi),\ \phi\in[0,2\pi), \tag{5.6}$$

and Ω_2 is the unit sphere, i.e., $R=1$. The Dirichlet data on $\partial\Omega_2$ is taken as (5.5) and the Neumann data (2.1d) is numerically simulated by solving the direct Dirichlet well-posed problem given by Eqs. (2.1a), (5.5), and (2.1c) with $\alpha=1$, when $\partial\Omega_1$ is given by (5.6), using the MFS with $M=N=\tilde{M}=\tilde{N}=43$. In order to avoid committing an inverse crime, the inverse solver is applied using $M=N=18, \tilde{M}=\tilde{N}=20$. In Fig. 18 we present the results obtained for no noise, no regularization and various numbers of iterations.

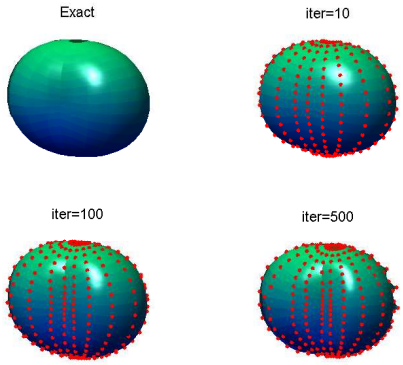

Figure 18: Example 5.4: Results for $M=N=18$, $\tilde{M}=\tilde{N}=20$, no noise and no regularization. The reconstructed values of r are presented as red dots.

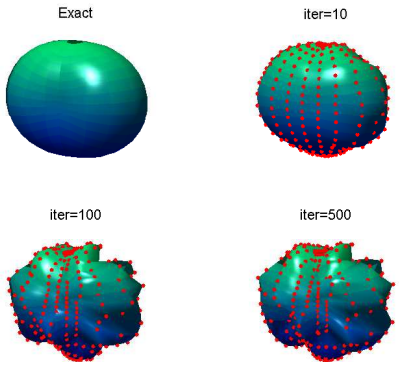

Figure 19: Example 5.4: Results for $M=N=18$, $\tilde{M}=\tilde{N}=20$, noise $p=5\%$ and no regularization.

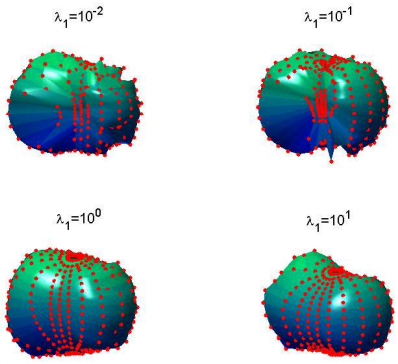

Figure 20: Example 5.4: Results for $M=N=18$, $\tilde{M}=\tilde{N}=20$, noise $p=5\%$ and regularization with λ_1.

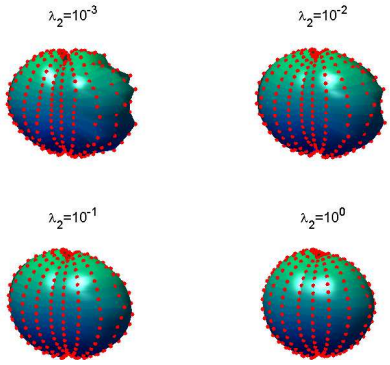

Figure 21: Example 5.4: Results for $M=N=18$, $\tilde{M}=\tilde{N}=20$, noise $p=5\%$ and regularization with λ_2.

The corresponding results for noise $p=5\%$ are presented in Fig. 19. In Figs. 20 and 21 we present the corresponding reconstructed surfaces for $p=5\%$ noise, obtained after 500 iterations, and various levels of regularization λ_1 with $\lambda_2=0$, and λ_2 with $\lambda_1=0$, respectively. The same conclusions as in Examples 5.2 and 5.3 are obtained.

6 Conclusions

The full merits of employing a meshless method, namely, ease of implementation, speed and accuracy, over more traditional domain or boundary discretisation methods become more evident in the solution of three-dimensional inverse problems. The numerical solution of such problems by the latter, mesh-dependent methods may become prohibitive due to the large number of times (iterations) an expensive direct solver has to be called. In particular, in this paper, a three-dimensional reconstruction of a void defect (rigid inclusion or cavity) embedded in a host material has been performed using a dynamic MFS with regularization. The coordinates of the centre of the assumed star-shaped void do not need to be prescribed as they are taken to be unknowns in the minimization process along with the location of the pseudo-boundaries on which the fictitious MFS sources are positioned. The numerically obtained results show that the numerical method is accurate (for no noise) and stable with respect to noise added in the input data.

Acknowledgments

The authors are grateful to the University of Cyprus, and the Romanian National Authority for Scientific Research, CNCS–UEFISCDI, project number PN–II–ID–PCE–2011–3–0521, for supporting this research.

References

[1] G. ALESSANDRINI AND E. DIBENEDETTO, *Determining* 2*-dimensional cracks in* 3*-dimensional bodies: uniqueness and stability*, Indiana Univ. Math. J., 46 (1997), pp. 1–82.

[2] C. J. S. ALVES, *On the choice of source points in the method of fundamental solutions*, Eng. Anal. Boundary Elements, 33 (2009), pp. 1348–1361.

[3] C. J. S. ALVES AND N. F. M. MARTINS, *Reconstruction of inclusions or cavities in potential problems using the MFS*, In: The Method of Fundamental Solutions–A Meshless Method, (C. S. Chen, A. Karageorghis and Y. S. Smyrlis, eds.), Dynamic Publishers Inc., Atlanta, 2008, pp. 51–73.

[4] D. BORMAN, D. B. INGHAM, B. T. JOHANSSON, AND D. LESNIC, *The method of fundamental solutions for detection of cavities in EIT*, J. Integral Equations Appl., 21 (2009), pp. 381–404.

[5] T. F. COLEMAN AND Y. LI, *On the convergence of interior-reflective Newton methods for nonlinear minimization subject to bounds*, Math. Programming, 67 (1994), pp. 189–224.

[6] T. F. COLEMAN AND Y. LI, *An interior trust region approach for nonlinear minimization subject to bounds*, SIAM J. Optimiz., 6 (1996), pp. 418–445.

[7] S. DAS AND A. MITRA, *An algorithm for the solution of inverse Laplace problems and its application in flaw identification in materials*, J. Comput. Phys., 99 (1992), pp. 99–105.

[8] E. A. DIVO, A. J. KASSAB, AND F. RODRÍGUEZ, *An efficient singular superposition technique for cavity detection and shape optimization*, Numer. Heat Transfer, Part B Fundamentals, 46 (2004), pp. 1–30.

[9] G. FAIRWEATHER AND A. KARAGEORGHIS, *The method of fundamental solutions for elliptic boundary value problems*, Adv. Comput. Math., 9 (1998), pp. 69–95.
[10] G. FAIRWEATHER AND R. L. JOHNSTON, *The method of fundamental solutions for problems in potential theory*, In: Treatment of Integral Equations by Numerical Methods, (C. T. H. Baker and G. F. Miller, eds.), Academic Press, London, 1982, pp. 349–359.
[11] P. GORZELAŃCZYK AND J. A. KOŁODZIEJ, *Some remarks concerning the shape of the source contour with application of the method of fundamental solutions to elastic torsion of prismatic rods*, Eng. Anal. Boundary Elements, 32 (2008), pp. 64–75.
[12] H. HADDAR AND R. KRESS, *Conformal mappings and inverse boundary value problems*, Inverse Problems, 21 (2005), pp. 935–953.
[13] P. C. HANSEN AND D. P. O'LEARY, *The use of the L-curve in the regularization of discrete ill-posed problems*, SIAM J. Sci. Comput., 14 (1993), pp. 1487–1503.
[14] P. C. HANSEN, Discrete Inverse Problems: Insight and Algorithms, SIAM, Philadelphia, 2010.
[15] C. K. HSIEH AND A. J. KASSAB, *A general method for the solution of inverse heat conduction problems with partially unknown system geometries*, Int. J. Heat Mass Transfer, 29 (1985), pp. 47–58.
[16] C. H. HUANG AND B.-H. CHAO, *Inverse geometry problem in identifying irregular boundary configurations*, Int. J. Heat Mass Transfer, 40 (1997), pp. 2045–2053.
[17] R. L. JOHNSTON AND G. FAIRWEATHER, *The method of fundamental solutions for problems in potential flow*, Appl. Math. Modelling, 8 (1984), pp. 265–270.
[18] A. KARAGEORGHIS AND D. LESNIC, *Detection of cavities using the method of fundamental solutions*, Inverse Problems Sci. Eng., 17 (2009), pp. 803–820.
[19] A. KARAGEORGHIS AND D. LESNIC, *The method of fundamental solutions for the inverse conductivity problem*, Inverse Problems Sci. Eng., 18 (2010), pp. 567–583.
[20] A. KARAGEORGHIS, D. LESNIC, AND L. MARIN, *A moving pseudo-boundary MFS for void detection*, Numer. Methods Partial Differential Equations, 29 (2013), pp. 935–960.
[21] A. KARAGEORGHIS, D. LESNIC, AND L. MARIN, *The MFS for inverse geometric problems*, In: Inverse Problems and Computational Mechanics (L. Marin, L. Munteanu, and V. Chiroiu, eds.), vol. 1, Editura Academiei Române, Bucharest, 2011, pp. 191–216.
[22] A. KARAGEORGHIS, D. LESNIC, AND L. MARIN, *A survey of applications of the MFS to inverse problems*, Inverse Problems Sci. Eng., 19 (2011), pp. 309–336.
[23] A. J. KASSAB AND C. K. HSIEH, *Application of infrared scanners and inverse heat conduction problems to infrared computerized axial tomography*, Rev. Scientific Instruments, 58 (1987), pp. 89–95.
[24] A. J. KASSAB AND J. POLLARD, *Automated algorithm for the nondestructive detection of subsurface cavities by the IR–CAT method*, J. Nondestructive Evaluation, 12 (1993), pp. 175–187.
[25] A. J. KASSAB AND J. POLLARD, *Automated cubic spline anchored grid pattern algorithm for the high resolution detection of subsurface cavities by the IR–CAT method*, Numer. Heat Transfer, Part B Fundamentals, 26 (1994), pp. 63–78.
[26] R. MATHON AND R. L. JOHNSTON, *The approximate solution of elliptic boundary–value problems by fundamental solutions*, SIAM J. Numer. Anal., 14 (1977), pp. 638–650.
[27] The MathWorks, Inc., 3 Apple Hill Dr., Natick, MA, Matlab.
[28] P. SERRANHO, *A hybrid method for inverse scattering for sound-soft obstacles in* $\mathbb{R}^3$, Inverse Problems Imaging, 1 (2007), pp. 691–712.